Energy-Efficient Locomotion Strategies and Performance Benchmarks using Point Mass Tensegrity Dynamics

Brian M. Cera, Anthony A. Thompson, and Alice M. Agogino

***Abstract*— This work introduces a novel 12-motor paired-cable actuation scheme to achieve rolling locomotion with a spherical tensegrity structure. Using a new point mass tensegrity dynamic formulation which we present, we utilize Model Predictive Control to generate optimal state-action trajectories for benchmark evaluation. In particular, locomotive performance is assessed based on the practical criteria of rolling speed, energy efficiency, and directional trajectory-tracking accuracy. Through simulation of 6-motor, 12-motor paired-cable, and 24-motor fully-actuated policies, we demonstrate that the 12-motor schema is superior to the 6-motor policy in all benchmark categories, comparable to the 24-motor policy in rolling speed, and is over five times more energy efficient than the fully-actuated 24-motor configuration.**

I. Introduction

Spherical tensegrity robots (tensegrities) are lightweight soft robots that are comprised of an elastic tension network that suspends and connects isolated rigid rods. A six-bar spherical tensegrity, shown in Figure 1, has six rigid rods held together by 24 series-elastic cables. Notably, the structural properties of compliant and low-weight tensegrities have proven to be advantageous in applications that involve high-impact loads and co-robotic cooperation with humans; potential applications for these tensegrity robots include space surface exploration rovers [1] and disaster response robotics. However, the performance and energy efficiencies of spherical tensegrity robots has yet to be evaluated for practical use cases in realistic scenarios.

Motion planning and optimal control for rolling locomotion has been a major driving force for tensegrity research in recent years. As a result, innovative approaches utilizing evolutionary algorithms, data-driven methods, and model-based optimal control have all been developed to control these novel complex robots. In particular, great emphasis has been placed on optimal performance with respect to rolling speed under non-ideal conditions and rough terrain, but less consideration has been made for practical implementation challenges such as energy efficiency, controllability, and directional trajectory-tracking accuracy.

The goals of this paper are to introduce and evaluate a novel 12-motor paired-cable actuation scheme for tensegrity locomotion, presenting new tools and benchmarks to adequately assess the performance of a tensegrity's mobility with respect to energy efficiency, rolling speed, and directional trajectory-tracking. Understandably, the values for these benchmarks heavily depend on the hardware design – the number of actuated cables, the actuators used, and which specific cables are controlled. Nevertheless, we believe that this preliminary exploration into these quantifiable metrics elucidates a greater understanding of practical tensegrity hardware and control policy design for future mobile tensegrity robots.

Fig. 1: Example of a spherical tensegrity robot, which locomotes through shape-shifting by controlling individual cable tensions. Each rod is 60 cm in length. [Photo courtesy of Squishy Robotics, Inc.]

In this paper, we first explore the new point mass tensegrity dynamics in great detail to demonstrate how equations of motion for the tensegrity dynamics can be easily constructed in a rigorous and procedural manner. Next, we outline our approach for motion planning through the use of Model Predictive Control (MPC) in conjunction with the new point mass formulation. Lastly, we demonstrate the approach's versatility by generating optimal state-action trajectories for different tensegrity actuation configurations and evaluating their locomotive performance using relevant benchmarks.

II. Prior Research

Various rolling locomotion control policies and actuation configurations for spherical tensegrities have been explored. Developments in single-cable actuation (i.e., where only one cable is actuated at a time) have chiefly relied on the design and analysis of hand-engineered control policies [2], [3]. In contrast, due to the nonlinear coupled dynamics of spherical tensegrity structures, multi-cable actuation (i.e., simultaneous actuation of all 24 cables) has proven to be a significantly more challenging task. Methods to explore multi-cable actuation primarily consist of Monte Carlo simulations and data-driven machine learning methods.

In recent years, research in multi-cable actuation for tensegrities, [4], [5], has found that locomotion by rolling can be achieved by shape-shifting to a desirable quasi-static

geometry that positions the center of mass outside of the support polygon, and recent advancements in continuous rolling locomotion for tensegrities have utilized deep reinforced learning [6], [7].

Finally, many tensegrity topologies and actuation configurations have been explored. Numerous designs of even just *spherical* tensegrities have demonstrated variability in the number of actuated cables, degrees of freedom, overall compliance, weight distribution, etc. Continuing on the innovations of these explorative hardware designs, this paper presents a novel 12-motor paired-cable actuation scheme and compares its performance to other schemes using standard benchmarks of energy efficiency, rolling speed, and directional trajectory-tracking.

III. The Six-bar Spherical Tensegrity Robot and Point Mass Dynamics

In this paper, we focus on the Class-1 spherical tensegrity topology. Specifically, Class-1 tensegrities are special tensegrity structures constructed with compressive bodies which bear no rigid joints and which are interconnected solely through series-elastic tensile elements. For this reason, Class-1 tensegrity dynamic equations of motion are well-structured and can be procedurally obtained when given a fixed set of parameters. In prior work [8], a minimal representation of the 3D rigid body dynamics for tensegrity systems is presented. While the reduced state-dimension of this minimal representation is advantageous, this particular formulation is susceptible to dynamic singularities, which can make robust and reliable motion planning and optimal control difficult. In this section, we present a new simplified point mass tensegrity dynamics representation which can be easily formulated for any Class-1 tensegrity structure.

For this point mass formulation, rather than representing true rigid body dynamics, we assume that the entirety of each rod's mass can be distributed between two point masses located at the ends of the rod, hereafter also refered to as *nodes*. Notably, this assumption's validity is largely dependent on the actual hardware design of the tensegrity robot; as an example, consider the tensegrity SUPERball [1] designed by the Intelligent Robotics Group at NASA Ames, which carries most of its mass closer to the ends of the rod, where heavier motor assemblies and electronics are housed. Thus, this point mass assumption can often be relatively accurate and greatly simplifies the formulation of tensegrity dynamic equations of motion, enabling rapid design and prototyping of new innovative topologies in simulation.

With these simplifying assumptions, we now consider only the positions, velocities, and accelerations of each point mass. We define vectors $\mathbf{p}$ and $\dot{\mathbf{p}} \in \mathbb{R}^{3N}$ containing the individual xyz positions and velocities of the N nodes as:

$$\mathbf{p} = [x_1, y_1, z_1, ..., x_N, y_N, z_N]^T \quad (1)$$

$$\dot{\mathbf{p}} = [\dot{x}_1, \dot{y}_1, \dot{z}_1, ..., \dot{x}_N, \dot{y}_N, \dot{z}_N]^T \quad (2)$$

Next, we assume that forces are imparted on each node purely through idealized two-force members (i.e., the rods and cables in pure compression/tension) or from the external environment (e.g., contact forces with the ground). For the remainder of this section, we discuss the dynamic formulation of the cable and rod forces intrinsic to tensegrity structures.

A. Series-Elastic Cable Forces

Forces which act on the nodes due to the spring-cables are calculated simply using Hookean approximations, with special consideration that no compressive forces can be applied through the cables:

$$\mathbf{F_{cables,j}} = max\{0, k_j(S_j - L_j)\} \quad (3)$$

Here k_j is the stiffness of the series-elastic cable j, S_j is the separation distance between the two end nodes attached to cable j, and L_j is the spring-cable assembly rest length (see Fig. 2).

Given a cable connectivity matrix $\mathbf{C} \in \mathbb{R}^{J\times N}$ (see [8] for details), with rows $\mathbf{C}_j$ that encode cable interconnections between pairs of nodes, we represent elements in the vector of cables forces, $\boldsymbol{\gamma} \in \mathbb{R}^J$, as:

$$\boldsymbol{\gamma}_j = \sqrt{2}k_j \cdot softplus\Big(\alpha_j, \beta\Big)\frac{\mathbf{z}_j}{\|\mathbf{z}_j\|_2} \quad \forall j \in \{1, ..., J\} \quad (4)$$

where variables $\mathbf{z}_j$ and α_j are defined as follows:

$$\mathbf{z}_j = -\left[\mathbf{C}_j^T\mathbf{C}_j \otimes \mathbf{I}_3\right]\mathbf{p}$$

$$\alpha_j = (S_j - L_j) = \sqrt{\frac{\mathbf{z}_j^T\mathbf{z}_j}{2}} - L_j$$

$\mathbf{z}_j \in \mathbb{R}^J$ is a sparse vector that contains the directional vector lying along the direction of the cable j. The *softplus* function above is a smooth approximation to the non-differentiable rectifier function (used in Eq. 3), approximating $max\{0, \alpha_i\}$ with tunable smoothness parameter β:

$$softplus(\alpha_j, \beta) := (\sqrt{\alpha_j^2 + \beta^2} + \alpha_j)/2 \geq 0 \quad (5)$$

In practice, this Lipschitz smooth approximation demonstrates better numerical stability in simulation and its continuously differentiable property is well-suited for calculating the locally-linearized dynamic models used in the receding horizon control methods discussed in later sections.

B. Rigid Body Constraint Forces

The other set of essential forces in tensegrity structures are the rigid body constraints, which constrain the nodal positions relative to each other and the environment.

Rather than model the rods using a linear-elastic model as with cable forces in the prior section, we instead adopt a constrained dynamics approach. The motivation behind

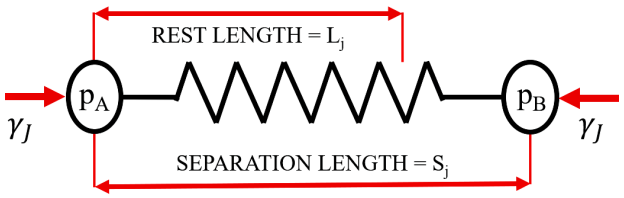

Fig. 2: Hookean linear-elastic model between two point masses.

this is that *penalty* or *energy barrier methods*, which rely on restorative forces to maintain rigid connections, necessitate large stiffness parameters and lead to stiff differential equations. Instead, the constraint forces we describe here neatly cancel out the components of the applied forces that violate rigid constraints at each timestep, creating accurate and numerically tractable dynamic simulations.

In our work, we adopt a similar approach to [9] and define constraint vectors, $\mathbf{G}(\mathbf{p})$ and $\dot{\mathbf{G}}(\mathbf{p}) \in \mathbb{R}^M$, to represent the implicit constraint functions and their time derivatives, where M is the number of active dynamic constraints. Each scalar element $\mathbf{G}_i(\mathbf{p})$ is a single implicit constraint function that is satisfied when equal to zero. If we assume that initial positions and velocities of the system satisfy dynamic constraints (i.e., $\mathbf{G}(\mathbf{p})$ = 0 and $\dot{\mathbf{G}}(\mathbf{p})$ = 0), then any forces which maintain legal accelerations (i.e., $\ddot{\mathbf{G}}(\mathbf{p})$ = 0) will be valid forces which satisfy all dynamic constraints.

We decompose the vector of *legal* forces $\mathbf{F}'$ which are ultimately applied to the particle masses into two components: $\mathbf{F}$, the total forces originally applied to the particle, and $\hat{\mathbf{F}}$ which are resultant constraint forces that cancel out any illegal accelerations. We also introduce the inverse-mass matrix $\mathbf{W}$, which contains the reciprocal of each particle's mass as elements along the diagonal. Thus, the legal acceleration condition can be written as:

$$\ddot{\mathbf{G}}(\mathbf{p}) = \left[\frac{\partial \dot{\mathbf{G}}(\mathbf{p})}{\partial \mathbf{p}}\right]\dot{\mathbf{p}} + \left[\frac{\partial \mathbf{G}(\mathbf{p})}{\partial \mathbf{p}}\right]\ddot{\mathbf{p}} \tag{6}$$

$$= \left[\frac{\partial \dot{\mathbf{G}}(\mathbf{p})}{\partial \mathbf{p}}\right]\dot{\mathbf{p}} + \left[\frac{\partial \mathbf{G}(\mathbf{p})}{\partial \mathbf{p}}\right]\mathbf{W}(\mathbf{F}+\hat{\mathbf{F}}) \;=\; \mathbf{0} \tag{7}$$

Simplifying notation of $\frac{\partial \mathbf{G}(\mathbf{p})}{\partial \mathbf{p}}$ and $\frac{\partial \dot{\mathbf{G}}(\mathbf{p})}{\partial \mathbf{p}}$ as matrices $\mathbf{J}(\mathbf{p})$ and $\dot{\mathbf{J}}(\mathbf{p})$, respectively, and dropping the matrices' explicit dependencies on $\mathbf{p}$, we rewrite:

$$\mathbf{JW}\hat{\mathbf{F}} \;=\; -\dot{\mathbf{J}}\dot{\mathbf{p}} - \mathbf{JWF} \tag{8}$$

$$\mathbf{JW}(\mathbf{J^T}\boldsymbol{\lambda}) \;=\; -\dot{\mathbf{J}}\dot{\mathbf{p}} - \mathbf{JWF} \tag{9}$$

where (Eq. 9) is a result of (Eq. 7) in combination with the principle of virtual work, which restricts constraint forces $\hat{\mathbf{F}}$ to lie in the subspace spanned by the constraint gradient vectors (i.e., the rows of $\frac{\partial \mathbf{G}(\mathbf{p})}{\partial \mathbf{p}}$). The vector $\boldsymbol{\lambda}$ of Lagrange multipliers determines how much of each constraint gradient is applied, providing a measure proportional to the reaction force applied due to the corresponding constraint. To prevent the accumulation of numerical drift, corrective stiffness and damping terms are appended to (Eq. 9):

$$\mathbf{JW}(\mathbf{J^T}\lambda) = -\dot{\mathbf{J}}\dot{\mathbf{p}} - \mathbf{JWF} - \mathbf{k_s}\mathbf{G} - \mathbf{k_d}\dot{\mathbf{G}} \tag{10}$$

As a concrete example, consider the constraint forces imposed by the rigid body connection between two endpoint nodes of a rod. Given nodal positions and velocities, rod length $L_{rod,q}$, and a rod connectivity matrix $\mathbf{R} \in \mathbb{R}^{Q\times N}$ with rows $\mathbf{R}_q$ that encode rod interconnections, we write an implicit rod constraint function constraining relative distance between nodal positions $\mathbf{p}_A$ and $\mathbf{p}_B$, the constraint function's respective time derivative, and their associated Jacobian matrices as:

$$\mathbf{G_i}(\mathbf{p}) \;=\; \|\mathbf{p_B} - \mathbf{p_A}\|_\mathbf{2}^\mathbf{2} - L_{rod,q}^2 \tag{11}$$

$$\;=\; \frac{\mathbf{1}}{\mathbf{2}}\mathbf{p^T}\left(\left[\mathbf{R_q^T R_q}\right]\otimes\mathbf{I_3}\right)^\mathbf{2}\mathbf{p} - L_{rod,q}^2 \tag{12}$$

$$\dot{\mathbf{G}}_\mathbf{i}(\mathbf{p}) \;=\; \mathbf{p^T}\left(\left[\mathbf{R_q^T R_q}\right]\otimes\mathbf{I_3}\right)^\mathbf{2}\dot{\mathbf{p}} \tag{13}$$

$$\mathbf{J_i}(\mathbf{p}) \;=\; \mathbf{p^T}\left(\left[\mathbf{R_q^T R_q}\right]\otimes\mathbf{I_3}\right)^\mathbf{2} \tag{14}$$

$$\dot{\mathbf{J}}_\mathbf{i}(\mathbf{p}) \;=\; \dot{\mathbf{p}}^\mathbf{T}\left(\left[\mathbf{R_q^T R_q}\right]\otimes\mathbf{I_3}\right)^\mathbf{2} \tag{15}$$

Given these implicit constraint functions which are obtained for each rod, we combine these results with the formulas in Section III-A to guarantee that nodal accelerations are realistically and stably simulated, with no pair-relative acceleration components lying along the axis of the rigid rods.

IV. Motion Planning using Model Predictive Control

Tensegrity motion planning and control can be overwhelmingly complex due to the high-dimensional, highly-coupled, nonlinear dynamics inherent to tensegrity robots. Generating optimal state-action trajectories (i.e., the control and time evolution of actuated cable rest lengths and the resulting dynamic states) can be a difficult task when considering the entirety of the 72-dimensional state-space and up to 24-dimensional action-space. Fortunately, we are able to leverage the well-structured dynamics of Class-1 tensegrities by importing the dynamic equations of motion derived in the Section III as optimization constraints for model-based receding horizon control such as Model Predictive Control (MPC).

In short, MPC is a control schema which iteratively solves a constrained optimization problem and implements only the first control input at the each timestep [10], [11]. The primary benefit of this control scheme is the ability to leverage dynamic models to optimize future behavior over finite time-horizons while also complying with state and input constraints, such as those defined by realistic safety and actuator limitations. Additionally, because MPC is an iterative algorithm, the approach is inherently robust to unforeseen disturbances.

In this work, we utilize MPC to automatically design and evaluate tensegrity locomotion actuation policies (i.e., how to optimally actuate cable rest lengths). The continuous dynamics of the robot are linearized about the robot's current state and discretized using a trapezoidal approximation:

$$\begin{bmatrix}\mathbf{p_{k+1}}\\ \dot{\mathbf{p}}_\mathbf{k+1}\end{bmatrix} = \begin{bmatrix}\mathbf{p_k}\\ \dot{\mathbf{p}}_\mathbf{k}\end{bmatrix} + \frac{dT}{2}\begin{bmatrix}\dot{\mathbf{p}}_\mathbf{k} + \dot{\mathbf{p}}_\mathbf{k+1}\\ 2\ddot{\mathbf{p}}_\mathbf{0} + \frac{\partial \ddot{\mathbf{p}}}{\partial \mathbf{x}}\tilde{\mathbf{x}}_\mathbf{k} + \frac{\partial \ddot{\mathbf{p}}}{\partial \mathbf{x}}\tilde{\mathbf{x}}_\mathbf{k+1}\end{bmatrix} \tag{16}$$

where dT is the simulation timestep, $\mathbf{x} \in \mathbb{R}^{96}$ is a concatenated vector of cable lengths and nodal position/velocity states, $\tilde{\mathbf{x}}_\mathbf{k}$ is the deviation about the linearization point $\mathbf{x_0}$, and $\ddot{\mathbf{p}}_\mathbf{0} \in \mathbb{R}^{3N}$ is the current state acceleration at $\mathbf{x} = \mathbf{x_0}$,

where $\ddot{\mathbf{p}}$ is calculated as follows:

$$\ddot{\mathbf{p}} = \mathbf{W}\Big(- \mathbf{J^T}(\mathbf{JWJ^T})^{-1}(\dot{\mathbf{J}}\dot{\mathbf{p}} - \mathbf{k_s G} - \mathbf{k_d}\dot{\mathbf{G}}) + (\mathbf{I} - \mathbf{J^T}(\mathbf{JWJ^T})^{-1}\mathbf{JW})(\sum_{\mathbf{i}}^{\mathbf{J}} \boldsymbol{\gamma}_\mathbf{i} + \mathbf{F_{ext}})\Big) \tag{17}$$

(Eq. 17) is obtained by combining the results of Sections III-A and III-B. Note, $\mathbf{F_{ext}}$ are the total forces applied to the tensegrity robot which are external to the system (e.g., ground contact reaction forces) and are calculated using damped linear-elastic collisions. These formulas are similar to those discussed in Section III-A, and thus a formal discussion of these external force calculations is excluded for the sake of brevity.

Using the derived linearized and discretized dynamics as optimization constraints, we minimize the following cost function:

$$\sum_{k=1}^{T} \boldsymbol{\psi}^{k-1} \left\{ -\theta_1 \sum_{i=1}^{N} \dot{\mathbf{p}}_i^T \mathbf{D} + \theta_2 \|\hat{\mathbf{L}}_\mathbf{k}\|_1 + \theta_3 \|\tilde{\mathbf{L}}_\mathbf{k}\|_1 \right\} \tag{18}$$

Here $\mathbf{D} \in \mathbb{R}^3$ is the desired direction of travel, T is the MPC finite-time horizon, and $\boldsymbol{\psi} < 1$ is a discount factor placing less weight on later states to account for linearization errors. Finally, $\theta_1, \theta_2, \theta_3$ are weighting parameters, and $\hat{\mathbf{L}}_\mathbf{k}$ and $\tilde{\mathbf{L}}_\mathbf{k} \in \mathbb{R}^J$ contain deviations of the k^{th}-step cable rest lengths about the neutral pretensioned lengths and initial lengths used for linearization, respectively. Combined, these cost terms reward rolling velocity in a desired direction while simultaneously penalizing cable rest length deviations from both initial pretensioned lengths and current rest lengths (i.e., $k = 1$), respectively, preventing the robot from excessive deformations and generating sparse motor actuation.

The convex cost function above and linear equality and inequality constraints from the dynamics, state/actuator limits, and initial conditions thus form a linear program which is easily minimized using any convex optimization solver. For this work, Gurobi Optimizer and YALMIP [12] were used in MATLAB to solve the optimization problem at each timestep iteration. Combined, these tools enable us to rapidly evaluate the novel 12-motor tensegrity actuation policy and its relative performance.

V. 12-motor paired-cable Actuation

Similar to the 24-motor actuation scheme, the 12-motor paired-cable actuation scheme controls all 24 cables in a spherical tensegrity; however, for the 12-motor scheme, two cables are coupled by a single motor. For this actuation scheme, a pair of cables meet at a single node – the retraction of one cable means the extension of the other cable in that pair. Thus, while all 24 cables are actuated, only 12 degrees of freedom exist in the system.

Interestingly, this new paired-cable schema has some practical advantages over its 24-motor schema counterpart. The most immediate advantages are that fewer parts are necessary, so the robot is less prone to mechanical failure, and that the tensegrity robot will weigh significantly less.

VI. Comparisons of Rolling Locomotion Strategies

In this final section, we discuss tensegrity rolling locomotion in detail and compare three cable-actuation schemes, each with varying degrees of control authority: 6-motor (underactuated), 12-motor (paired-actuation), and 24-motor (full-actuation) schema. In particular, these actuation schema vary the number of cables that are driven by motor actuators and consequently which cables remain as passive tensile elements. As a result, we demonstrate that greater control authority can provide improved performance at the cost of additional hardware and controller complexity.

In the results that follow, we utilize MPC with the dynamic constraints introduced earlier to generate optimal state-action trajectories for evaluation. Notably, the simulation model parameters used in these experiments are based on actual hardware parameters of the tensegrity robot shown in Fig. 1:

Physical Parameters	Value
Rod Length	60 cm
Rod Mass	500 g
Cable Stiffness	400 N/m
Pretension	50 N
Max. Cable Linear Velocity	20 cm/s

For the remainder of this section, we discuss various characteristic properties of tensegrity locomotion. First, we use the 24-motor fully-actuated scheme to illustrate hardware and controller design considerations that are unique to compliant tensegrity rolling locomotion; namely, we assert that tensegrity stiffness and initial pretension are important hardware and controller design hyperparameters. We conclude this section by evaluating the nominal performance of the three common actuation schema introduced above with respect to relevant performance metrics such as speed, directional trajectory-tracking, and energy efficiency.

A. Effective Tensegrity Stiffness and Pretension

The inherent compliance of tensegrity structures serves as a benefit with regards to mechanical robustness, particularly in the structure's impact-resilience, natural force distribution, and lack of mechanical stress concentrators. On the other hand, the resulting oscillatory dynamic behavior complicates optimal control policy design. In this section, we present results obtained when adjusting overall tensegrity stiffness and pretension (i.e., the stiffness and initial pretension of all individual series-elastic tension elements) and assess its broader effects on rolling locomotion. For this evaluation, we examine the relative dynamic behavior of the robot as we adjust the overall stiffness and pretension of the fully-actuated robot between 50% and 200% of the nominal values of 400 N/m and 50 N. The simulation parameters we use for MPC are as follows:

Timesteps	dT	T	ψ	θ_1	θ_2	θ_3
500	0.01	10	0.95	1.0	3.0	3.0

As we can see from the results in Fig. 3, greater overall stiffness in the robot leads to better rolling performance

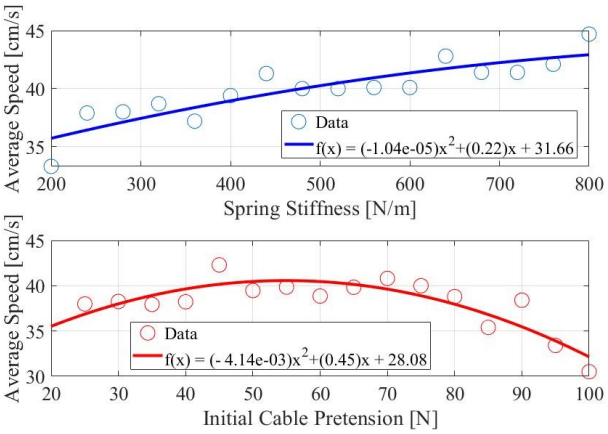

Fig. 3: A comparison of average rolling speeds vs. overall stiffness and initial cable pretension, with 24-motor scheme. Near-linear fitting curves highlight the overall trends.

with the receding horizon controller. Similarly, performance improves as initial pretension of the robot increases, before dropping off. Intuitively, these results match expectations, as greater stiffness creates less oscillatory dynamics which the controller is unable to account for, due to the low controller timestep of 0.01 seconds. Greater stiffness and pretension ensures that the robot is less likely to drastically deform in a detrimental manner by giving immediate and precise control over the state of the robot with less actuation input. That said, the results illustrate that excessively large pretensions can also negatively affect tensegrity locomotion. One possible explanation for this observed behavior is that excessively large pretensions during the initial state require more actuation before the robot can sufficiently change its shape and enter a stable dynamic rolling gait.

Effectively, these results support that tensegrity robots become easier to control using inexpensive and computationally-limited microcontrollers as the tensegrity dynamics approach rigid-like behavior; lower update frequencies are less of an issue as state uncertainty due to compliance in the robot decreases. Unfortunately, greater stiffness in the overall robot also leads to prohibitively high torque and power requirements on the motor actuators, an issue we discuss in greater detail later in Section VI-C.

B. Speed and Directional Control

Next, we compare the performance of the three actuation schema presented earlier (i.e., 6-motor, 24-motor fully-actuated, and 12-motor paired-actuated) with respect to average rolling speed and directional trajectory control. In this section, we discuss the advantages that are provided through the use of additional cable actuators.

As an illustrative example, we examine the average rolling speed of the robot under each of the three actuation policies, maximizing rolling velocity in a specified direction. To get a more representative average speed, the total number of timesteps we simulate is doubled from the previous section.

From the trials shown in Fig. 4, it is clear that the greater control authority, afforded by more actuated cables for 24-cable policies, enables the robot to accomplish locomotion

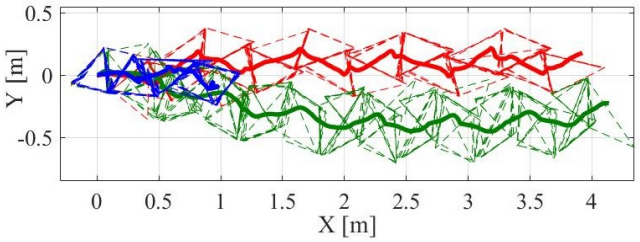

Fig. 4: Footprint trails of the robot starting at the origin and rolling in the +X-direction for 10 seconds using 24-motor fully-actuated (red), 12-motor paired-actuated (green), and 6-motor actuation policies (blue). Solid lines indicate the robot's center of mass and dotted lines indicate supporting polygons in contact with the ground.

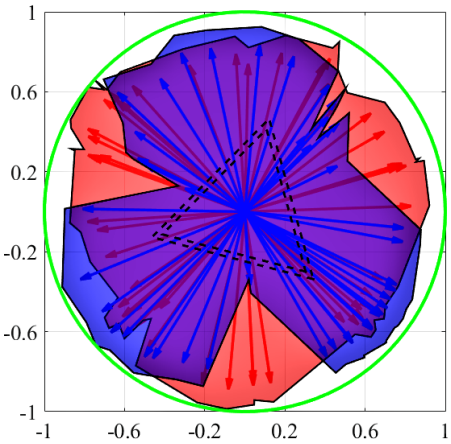

Fig. 5: Plot showing normalized average speeds in various directions, starting from an identical initial state (base polygon outlined in dashed black lines). Red represents results for fully-actuated 24-motor scheme, and blue represents 12-motor paired-cable actuation scheme.

tasks that the 6-motor variant simply cannot complete. In this simple illustrative example, we see that, given the limited degrees of freedom, the 6-motor actuation scheme is simply unable to roll in the desired direction and becomes stuck as it attempts to do so. That said, both the fully-actuated and paired-actuated 24-cable policies were able to perform reasonably well. Naturally, however, the greater controllability of the fully-actuated system allows for greater directional trajectory-tracking accuracy along the +X-axis. In Fig. 5, this improved directional controllability is highlighted as we evaluate the robot's performance in any-direction rolling. In this figure, average rolling speeds are normalized by the fastest experimental trial, so that all arrows lie within the unit circle. In particular, it is shown that while both the 24-motor and 12-motor schemes can achieve reasonable top speeds, the lesser degree of freedom provided by the paired-cable schema (i.e., 12 motor actuators rather than 24), precludes good performance in *all* directions.

To conclude, we summarize the relative performance of each actuation policy, stating the average speeds of each scheme followed by a normalized value – average speed divided by the product of the rod length of the spherical tensegrity design and the maximum linear velocity of the

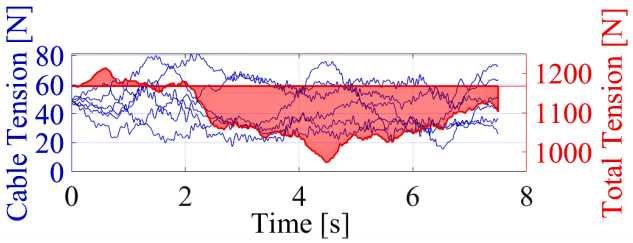

Fig. 6: Cable tensions for 6 of 24 cables (left) and total tension (right) for 24-motor rolling locomotion. Note, in attaining maximum rolling speed, total tension in the robot remains below the initial pretensioned state after some time (2 seconds).

motors. Importantly, we believe that this normalization will simplify comparisons of performance across different hardware configurations and tensegrity topologies.

Schema	6-motor	12-motor	24-motor
Avg. Speed	18.1 cm/s	37.9 cm/s	38.2 cm/s
Norm. Speed	1.51e-02	3.16e-02	3.18e-02

C. Energy Efficiency

In this final section, we briefly discuss the energy efficiency of both the 12-motor paired-cable and 24-motor actuation schema. As shown in the previous section, comparable performance for maximum rolling speeds is achieved for both 12-motor and 24-motor actuation schemes. However, as demonstrated, 12-motor actuation does sacrifice some degree of maneuverability due to the lesser control authority granted. Nevertheless, in this section, we provide a compelling motivator for the 12-motor variant on the basis of energy efficiency.

We consider a simplified model of energy-costs which relates tension in the robot to power consumed by the motors. Specifically, cable tensions (see Fig. 6) are directly related to load torques on the motor and correlates to current draw and power consumption. If we assume 65% efficient motors, the average Cost of Transport (i.e., energy divided by mass times distance traveled) over 100 trials are **159.9** and **30.7** for 24-motor and 12-motor actuation schema, respectively. Notably, the exceptional Cost of Transport is on par with the locomotive efficiency of many animals found in nature [13]. Specifically, the unique paired-cable mechanism is able to leverage complementary tensions of each cable-pair such that the motor does minimal work under normal operating conditions. Thus, while some degree of maneuverability is lost, the energy efficiency gains makes a 12-motor paired-cable actuation schema an enticing candidate tensegrity robot design.

VII. Conclusion

In conclusion, we have introduced a novel 12-motor paired-cable actuation policy and the practical benefits it holds over the more complex, fully-actuated 24-motor configuration. In formulating the point mass dynamics and simulating the optimal MPC state-action trajectories for the 6-motor, 12-motor, and 24-motor actuation policies, we were able to evaluate the relative performances of each scheme. As an insightful result, we demonstrated that the new 12-motor paired-cable scheme is capable of competitive rolling speeds and is over five times more energy efficient than the other two configurations; however, since the 24-motor scheme has greater control authority, it has better directional trajectory-tracking than both the 6-motor and 12-motor variants. Finally, we look forward to using these tools to investigate even more novel tensegrity topologies and to applying the new paired-cable actuation policy on new robot hardware for empirical results.

Acknowledgement

The authors thank the engineers at Squishy Robotics, Inc. for lending their tensegrity hardware for this analysis, which was partially funded by NSF SBIR Phase I grant #1747189.

References

[1] V. SunSpiral, A. Agogino, and D. Atkinson, "Super ball bot-structures for planetary landing and exploration, niac phase 2 final report," 2015.

[2] K. Kim, A. K. Agogino, D. Moon, L. Taneja, A. Toghyan, B. Dehghani, V. SunSpiral, and A. M. Agogino, "Rapid prototyping design and control of tensegrity soft robot for locomotion," in *2014 IEEE International Conference on Robotics and Biomimetics (ROBIO 2014)*. IEEE, 2014, pp. 7–14.

[3] L.-H. Chen, B. Cera, E. L. Zhu, R. Edmunds, F. Rice, A. Bronars, E. Tang, S. R. Malekshahi, O. Romero, A. K. Agogino *et al.*, "Inclined surface locomotion strategies for spherical tensegrity robots," in *2017 IEEE/RSJ International Conference on Intelligent Robots and Systems (IROS)*. IEEE, 2017, pp. 4976–4981.

[4] K. Kim, A. K. Agogino, A. Toghyan, D. Moon, L. Taneja, and A. M. Agogino, "Robust learning of tensegrity robot control for locomotion through form-finding," in *2015 IEEE/RSJ International Conference on Intelligent Robots and Systems (IROS)*. IEEE, 2015, pp. 5824–5831.

[5] C. Paul, F. J. Valero-Cuevas, and H. Lipson, "Design and control of tensegrity robots for locomotion," *IEEE Transactions on Robotics*, vol. 22, no. 5, pp. 944–957, 2006.

[6] M. Zhang, X. Geng, J. Bruce, K. Caluwaerts, M. Vespignani, V. SunSpiral, P. Abbeel, and S. Levine, "Deep reinforcement learning for tensegrity robot locomotion," in *2017 IEEE International Conference on Robotics and Automation (ICRA)*. IEEE, 2017, pp. 634–641.

[7] J. Luo, R. Edmunds, F. Rice, and A. M. Agogino, "Tensegrity robot locomotion under limited sensory inputs via deep reinforcement learning," in *2018 IEEE International Conference on Robotics and Automation (ICRA)*. IEEE, 2018, pp. 6260–6267.

[8] B. Cera and A. M. Agogino, "Multi-cable rolling locomotion with spherical tensegrities using model predictive control and deep learning," in *2018 IEEE/RSJ International Conference on Intelligent Robots and Systems (IROS)*. IEEE, 2018, pp. 1–9.

[9] A. Witkin, "Physically based modeling–constraint dynamics," *ACM SIGGRAPH 2001 Course Notes*, 2001.

[10] C. E. Garcia, D. M. Prett, and M. Morari, "Model predictive control: theory and practicea survey," *Automatica*, vol. 25, no. 3, pp. 335–348, 1989.

[11] J. B. Rawlings and D. Q. Mayne, *Model predictive control: Theory and design*. Nob Hill Pub. Madison, Wisconsin, 2009.

[12] J. Löfberg, "Yalmip: A toolbox for modeling and optimization in matlab," in *Proceedings of the CACSD Conference*, vol. 3. Taipei, Taiwan, 2004.

[13] R. J. Full and M. S. Tu, "Mechanics of a rapid running insect: two-, four-and six-legged locomotion," *Journal of Experimental Biology*, vol. 156, no. 1, pp. 215–231, 1991.